sustainability

Article

Decadal Change of Meiyu Onset over Yangtze River and Its Causes

Yong Qian [1], Pangchi Hsu [1,*], Zhen Fu [1], Yunyun Liu [2] and Qiaoping Li [3]

1 Key Laboratory of Meteorological Disaster of Ministry of Education/CIC-FEMD/ILCEC, Nanjing University of Information Science & Technology, Nanjing 210044, China; qiany@nuist.edu.cn (Y.Q.); fuzhen.nuist@gmail.com (Z.F.)
2 Laboratory of Climate Studies, National Climate Center, China Meteorological Administration, Beijing 100081, China; liuyuny@cma.gov.cn
3 CMA Earth System Modeling and Prediction Centre, China Meteorological Administration, Beijing 100081, China; liqp@cma.gov.cn
* Correspondence: pangchi@nuist.edu.cn

Abstract: Meiyu onset marks the beginning of the rainfall season in the densely populated Yangtze River Basin, whether the Meiyu initiates early or late in June, and thus has a profound effect on the several hundred million people living there. Applying a Bayesian change-point analysis to data from 1960–2014, we objectively detected an abrupt change of Meiyu onset around 2002. The Meiyu onset date averaged over 2002–2014 was 19 June, delayed by about two weeks compared to that of 1989–2001 (6 June). This decadal change is attributable to the distinct amplitude of moisture transport toward the Yangtze River Basin induced by the changes in climatological intraseasonal oscillation (CISO). The CISO emerges as the annual cycle interacts with the transient intraseasonal perturbations. The wet/dry phases of the CISO are consistent with the climatological active/break stages of the East Asian summer monsoon. In early June, the northwestward-propagating CISO convective/cyclonic anomalies over the western North Pacific (WNP) show weaker amplitude during the earlier-onset epoch compared to the delayed-onset epoch. Thus, relative to the delayed onset epoch, a quasi-barotropic anticyclonic CISO anomaly appears over the WNP in early June during the earlier-onset years. This anticyclonic anomaly was conducive to the westward extension of the WNP subtropical high, conveying warm, moist air from the tropics toward the Yangtze River Basin for the rainy season onset. Model experiments suggest that the decadal changes in WNP CISO intensity were associated with the epochal changes in large-scale background circulation and sea surface temperature over the WNP.

Keywords: Meiyu onset; Yangtze River Basin; decadal variability; intraseasonal oscillation; western North Pacific

Citation: Qian, Y.; Hsu, P.; Fu, Z.; Liu, Y.; Li, Q. Decadal Change of Meiyu Onset over Yangtze River and Its Causes. *Sustainability* **2022**, *14*, 5085. https://doi.org/10.3390/su14095085

Academic Editors: Xuguang Sun, Zhiwei Zhu, Qing Bao and Youcun Qi

Received: 18 March 2022
Accepted: 21 April 2022
Published: 23 April 2022

1. Introduction

The major rainy season of the East Asian summer monsoon (EASM), known as Meiyu in China, Baiu in Japan, and Changma in south Korea, is caused by a quasi-stationary rain belt in early summer (mid-June to mid-July), which brings downpours that account for more than half of the annual precipitation in these regions [1]. As the critical suppliers of water resources, the onset, duration, and intensity of the Meiyu season exert enormous impacts on socioeconomic development and human life over the densely populated regions in East Asia. For example, an earlier onset combined with a delayed retreat, together with unusually intensified and persistent rainfall events, was recorded in the Meiyu season of 2020, which caused the worst flooding in China in recent decades with more than 140 dead or missing and USD 11.75 billion economic losses by mid-July [2]. Therefore, advancing our understanding of the critical factors controlling the changes in Meiyu characteristics is the basis to improve the fidelity of Meiyu prediction and thus reduce flood disasters [3].

The major components of the EASM, such as the western North Pacific (WNP) subtropical high, the upper-level South Asian high, the cold vortex in northern China, and the westerly jet over Eurasia, may affect the EASM rainfall pattern and thus Meiyu activity [3–8]. Previous studies found that the intensity of Meiyu precipitation is regulated by moisture transport by the low-level southwesterly of the WNP subtropical high and the ascending air mass motions induced by the westerly jet and South Asian high [1,4–6]. In contrast, the onset of Meiyu is associated with the northward jump of monsoonal circulations, which is linked to the evolution of the climatological intraseasonal oscillation (CISO) over the WNP [7,9,10]. The CISO originates when the transient intraseasonal perturbations are modulated by the annual cycle [9]. It reveals a northward-propagating feature over the WNP-EASM regions; the wet/dry phases of the CISO are consistent with the climatological active/break stages of EASM [7,9,11].

Meiyu intensity, onset, retreat, and duration exhibit significant interannual and decadal variations. Numerous studies unveiled the influences of different climate modes, such as the El Niño, Pacific decadal oscillation (PDO) and Atlantic multidecadal oscillation (AMO), on EASM rainfall patterns, including Meiyu [3,12–14]. Most studies investigated the interannual-to-decadal variability in total rainfall amount or intensity of Meiyu [13,14], while fewer studies paid attention to the changes in Meiyu onset dates. With a focus on the interannual variation in Meiyu onset date, Li et al. [15] identified the evolution of the South Asian anticyclone in April as a precursory signal for the Meiyu onset timing. Yao et al. [16] pointed out that the interannual variability of Meiyu onset is related to the spring intraseasonal oscillation (ISO) amplitude modulated by different types of El Niño sea surface temperature (SST) patterns. So far, however, there are limited discussions on whether the Meiyu onset reveals any regime shift at the decadal timescale, and, if so, what causes this change in timing.

In Section 2, we introduce the data and methods used in this study. In Section 3, we first objectively detect the change-point occurrence of Meiyu onset over the past decades. Then, we compare the differences in large-scale circulation, convection and CISO associated with Meiyu onset between the earlier- and delayed-onset epochs. To support the observational findings and explore the mechanisms responsible for the decadal changes in the CISO associated with Meiyu onset, a set of model experiments are used Discussion and conclusions are given in Section 4.

2. Data and Methods

Daily mean large-scale atmospheric conditions, including 3D wind, specific humidity, geopotential height, and surface pressure, at $2.5^\circ \times 2.5^\circ$ resolution are obtained from the European Centre for Medium-Range Weather Forecasts (ECMWF) Interim Reanalysis (ERA-Interim) [17]. We also use daily outgoing longwave radiation (OLR) from the National Oceanic and Atmospheric Administration's polar-orbiting satellites [18] and daily SST from the Optimum Interpolation Sea Surface Temperature (OISST) [19]. The resolutions of OLR and SST are 2.5° and 0.25°, respectively.

The Meiyu data over the Yangtze River, including onset date, retreat date and precipitation, are obtained from the National Climate Center of China Meteorological Administration. The onset of Yangtze River Meiyu is determined by several criteria related to large-scale monsoon circulations and continuous rainfall amounts over the Yangtze River Basin [3].

A Bayesian paradigm is utilized to objectively detect the occurrence of a regime shift. Detailed formula and steps of the Bayesian change-point analysis can be found in Chu and Zhao [20,21]. Here, we briefly summarize its characteristics and advantage: (1) a Poisson process is used to model the time series of each variable, with the Poisson intensity codified by its gamma distribution; and (2) to determine the posterior probability of the shift in time, a hierarchical (i.e., structural layers) approach involving three layers (data, parameters, and hypothesis) is used. Rather than a deterministic estimate of the change-point location, the Bayesian analysis gives probability information about change points. This is an advantage over the deterministic approach since the uncertainty inherent in statistical inferences is quantitatively reflected in the probability statement [21,22].

To examine the sensitivity of change-point analysis results, we used another method named the sequential *t*-test analysis of regime shifts (STARS) [23] for detecting possible regime shifts in Meiyu onset. Compared to the Bayesian change-point analysis, for a Poisson process, the STARS has no strict rules for selecting parameters and does not require a very long/complete time series of a variable for detection.

Following Rodionov [23], the Student's *t*-test is applied to determine whether the difference between two subsequent regimes ($diff$) is statistically significant.

$$diff = t_{2l-2,\ p}\sqrt{2\sigma_l^2/l}$$

where σ_l^2 is the average variance for all running intervals with length l (i.e., the cut-off length of the regimes), and $t_{2l-2,\ p}$ is the value of t-distribution with $2l-2$ degrees of freedom at a specified probability level p (p = 0.05 in this study). If the current value (x_i) appears to exceed $\overline{x}_{R1} \pm diff$, in which $\overline{x}_{R1} = \sum_{i=1}^{l} x_i$, it is considered as a possible start point j of the new regime $R2$. For this potential regime shift point j, the regime shift index (RSI) is calculated as follows,

$$\mathrm{RSI}_{i,j} = \sum_{i=j}^{j+m} \frac{x_i - (\overline{x}_{R1} + diff)}{l\sigma_l},\ m = 0,\ 1,\ \ldots,\ l-1.$$

If the RSI keeps the same sign as the one at time point j, it indicates a significant regime shift point. The greater the RSI value is, the more abrupt the change is.

For the analysis of the CISO during the Meiyu onset period, the Lanczos bandpass filter was applied to the daily OLR and wind fields to extract the transient ISO variability with a period of 20–90 days. The Lanczos bandpass filter is a Fourier method of filtering digital data [24]. With the advantage of relatively simple but inexpensive computation, the Lanczos bandpass filter is widely used when extracting weather/climate systems at different timescales. The daily mean of transient ISO was taken over individual epochs of interest to obtain the components of the CISO for different climate regimes. Note that the behaviors of the CISO remain consistent when they are derived from the bandpass-filtered climatological daily mean data.

The ECHAM4 atmospheric general circulation model (AGCM), developed by the Max Planck Institute for Meteorology [25], is used to explore the ISO changes in response to regional SST anomalies. Although it is not the newest version of the ECHAM, the ECHAM4 AGCM has been widely utilized in ISO-related studies because of its superiority in ISO simulations [7,26–28].

3. Results

3.1. Decadal Changes in Meiyu Onset and Associated Circulation Modulation

Meiyu onset during 1960–2014 shows multiple timescale variations, including interannual and decadal variability (Figure 1a). We can see one or a few years with earlier onset of the Meiyu season (blue bars), followed by some years with late onset (red bars). The interannual changes in Meiyu onset were closely linked with evolution of ENSO phases [3]. Besides the interannual variability, the Meiyu onset timing shows decadal variability, characterized by earlier onsets during the late-1980s to the late-1990s and by delayed onsets during other decades (mid-1960s to mid-1970s, early-2000s to early-2010s). To objectively detect the decadal changes in Meiyu onset, we apply the Bayesian change-point analysis to estimate the posterior probability of each observation as a potential change point during 1960–2014 (gray bars at the bottom of Figure 1a). The posterior probability shown in the bottom panel of Figure 1a indicates the probability of a change point occurring in a specific year. Since only one change point was detected in the time series, the maximum probability measured in 2002 suggests that a regime shift likely occurred in 2002. Note that the change point in 2002 remained the same when we extended the data to 2018 (not shown). We confirmed these results (not shown) by using sequential algorithm-based statistical analysis [23]. After testing various parameters in STARS, we found that the year 2002 was robustly detected as a change point for Meiyu onset when the cut-off length was 8–15 (Figure 2). Our change-point analysis results, based on STARS, also suggest that the cut-off length of 13 years for earlier and latter regimes is appropriate, because the RSI maximizes when l = 13 (Figure 2).

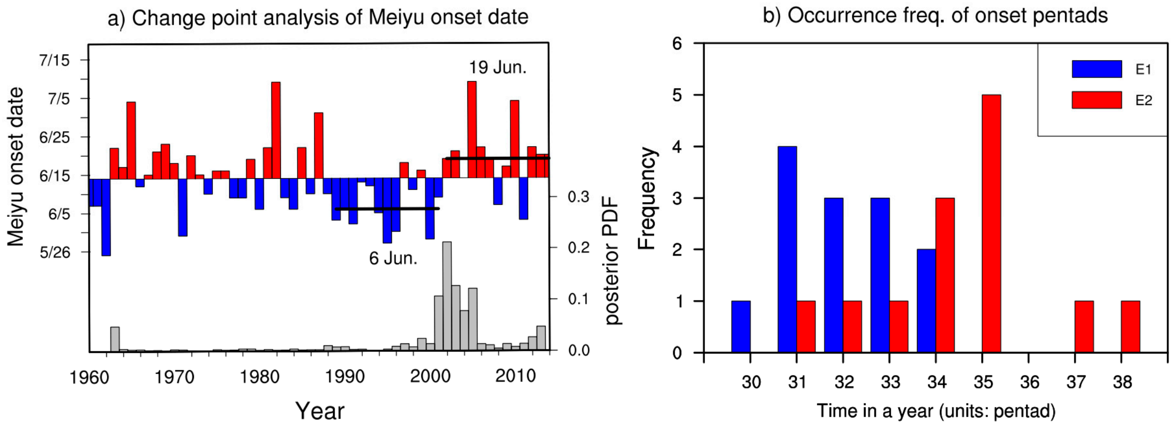

Figure 1. Decadal change of Meiyu onset over Yangtze River Basin in China. (**a**) Time series of Yangtze River Meiyu onset date during 1960–2014 relative to the climatological mean onset date of 14 June. Blue and red bars mark the early and delayed onset years, respectively. Black lines denote the epochal averages of Meiyu onset date of 6 June for 1989–2001 and of 19 June for 2002–2014. The posterior probability mass function of the change point as a function of time (year) is displayed at the bottom. (**b**) Frequency of onset occurrence in each pentad for E1 (1989–2001; blue bars) and E2 (2002–2014; red bars).

Using equal length periods before (1989–2001) and after (2002–2014) the change point, we compared the averaged Meiyu onset dates (black lines in Figure 1a) and found a significant contrast between the two. The onset date averaged over the earlier epoch (referred to as E1) is 6 June, while it was delayed by about two weeks (19 June) in the recent epoch (referred to as E2). This epochal change is statistically significant at the 95% confidence level according to two-tailed t-test (Table 1). Previous studies documented that an earlier onset was generally accompanied by an extended and enhanced rainy (Meiyu) season, leading to disastrous flooding [1]. Based on the comparison between the two epochs before and after the change point, we found that a longer and more intense Meiyu season was recorded in E1 than in E2. However, the epochal changes in retreat date, length, total precipitation amount, and intensity of Meiyu are not statistically significant (Table 1).

Table 1. (Top to bottom) Meiyu onset date, retreat, precipitation amount, and intensity averaged over E1 (1989–2001) and E2 (2002–2014), and their difference (E1 minus E2).

Meiyu Features	E1 (1989–2001)	E2 (2002–2014)	Epochal Diff. (E1-E2)
Onset date	6 June	19 June	−13 *
Retreat date	11 July	17 July	−6
Meiyu precipitation amount	324.6	259.8	64.8
Precipitation intensity	7.78	7.11	0.67

Note: The Meiyu precipitation amount (units: mm) is defined as the total precipitation accumulated from onset date to retreat date. The intensity of Meiyu precipitation measures the average precipitation amount per day (units: mm day^{-1}). Asterisk indicates that the epochal difference between E1 and E2 is statistically significant at the 95% confidence level.

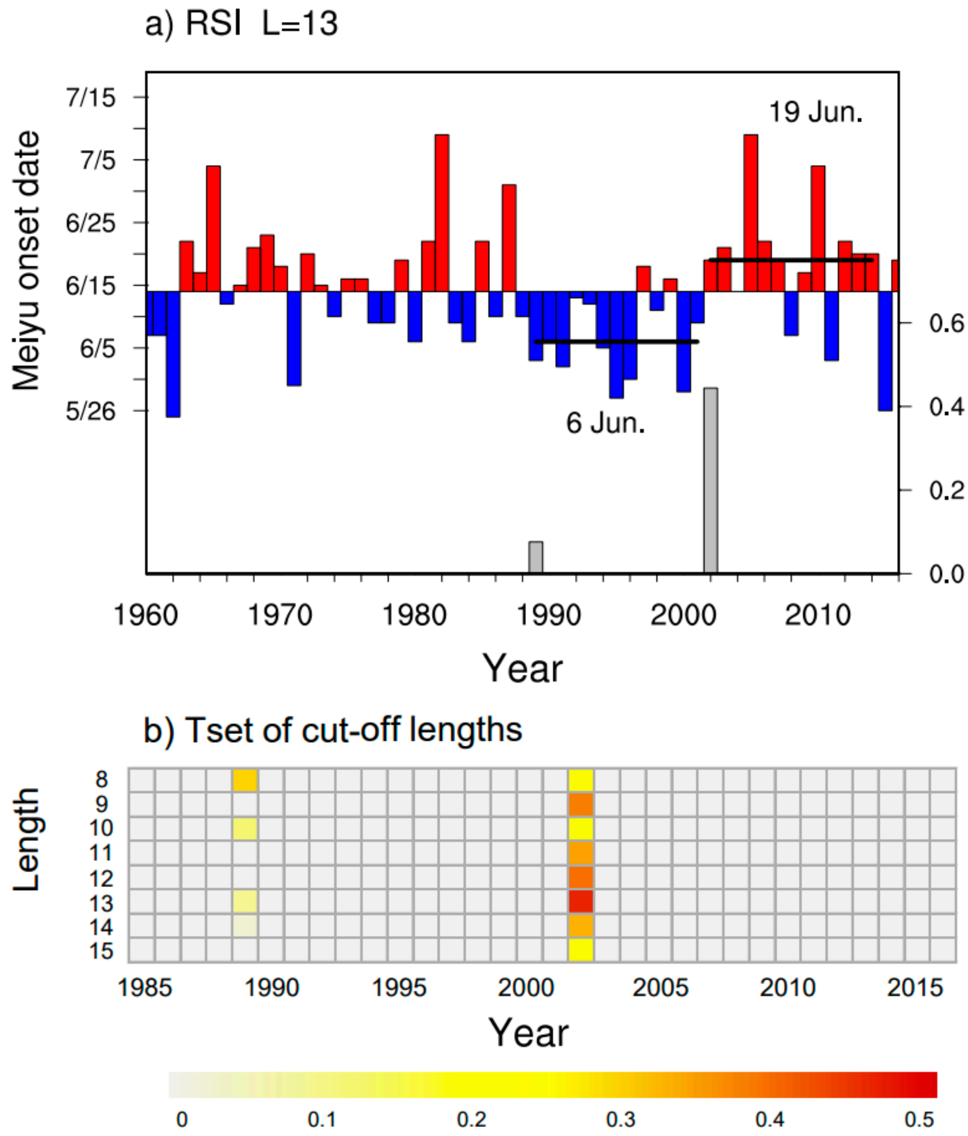

Figure 2. (**a**) Same as in Figure 1 but for the results detected by STARS method. The RSI values of the change point as a function of time (year) is displayed at the bottom. (**b**) Heat map of different RSI values when different cut-off lengths were used during 1985–2016.

During E1, the Meiyu onset concentrated among pentads 30–34, with most (10/13) of the cases occurring in pentads 31–33 (blue bars in Figure 1b). In contrast, the Meiyu in E2 had a small probability of initiating before pentad 34 (red bars in Figure 1b). We attempt to address why the Meiyu onset in E1 occurred during pentads 30–33 but was much delayed in E2. To understand what caused the decadal change in Meiyu onset, we examine the large-scale features of convection, circulation and moisture transport during pentads 30–33 when Meiyu tended to initiate in E1, but not in E2. Figure 3 shows evolutions of convection, low-level moisture flux and the extent of the WNP subtropical high during earlier- and delayed-onset epochs and their differences. In both epochs, the suppressed convection associated with the WNP subtropical high prevailed over the WNP, while a deep convection along with southwesterly moisture transport appeared over the Bay of Bengal, characterizing the major components of the EASM in the lower troposphere (Figure 3a–h).

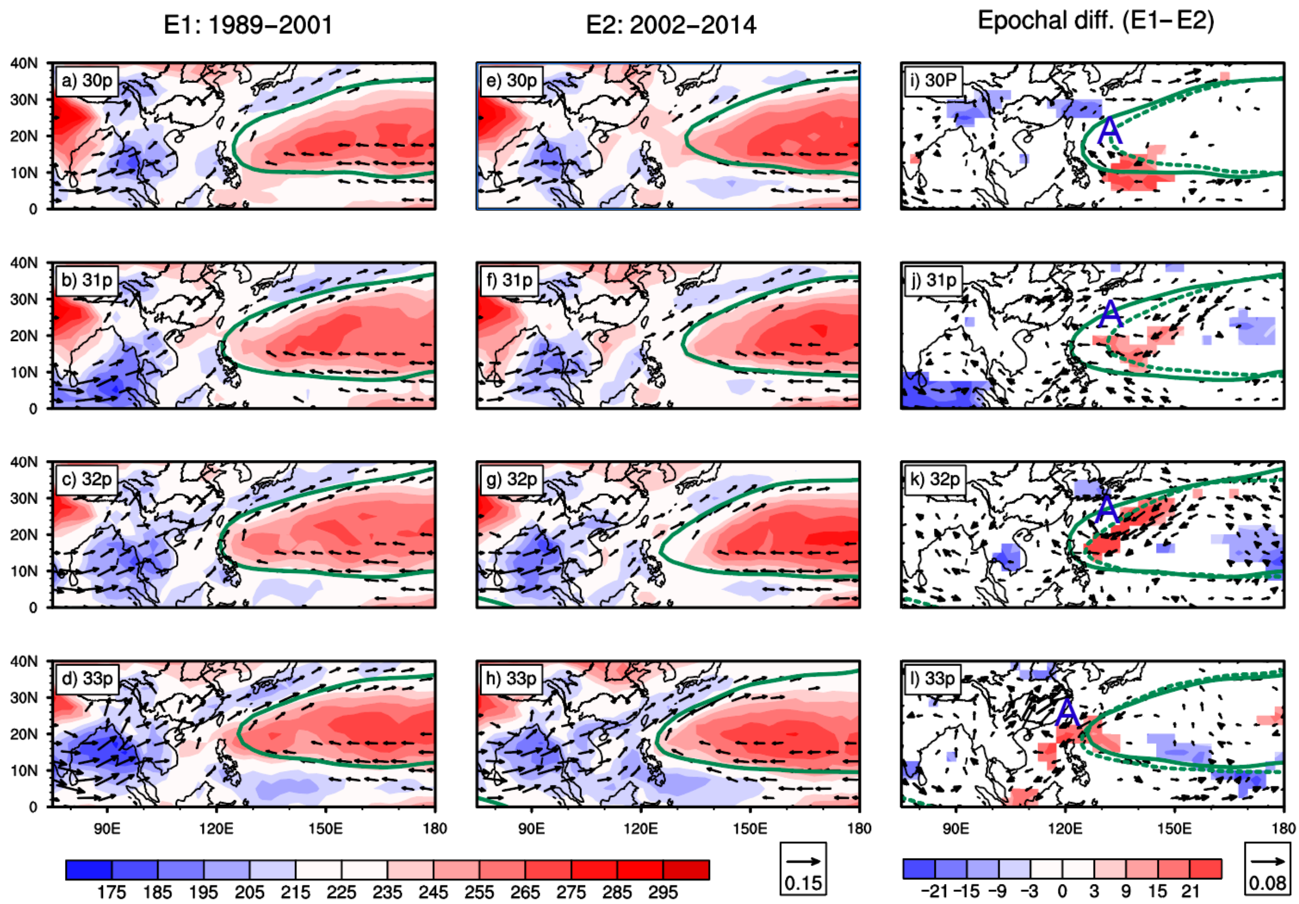

Figure 3. Composites of outgoing long-wave radiation (OLR; shading; units: W m^{-2}), 850-hPa moisture flux (vector; units: m s^{-1}) and 700-hPa stream function with the value of 0 m^2s^{-1} (green curve) in (**a**) pentad 30, (**b**) pentad 31, (**c**) pentad 32, and (**d**) pentad 33 during E1 (1989–2001). (**e**–**h**) and (**i**–**l**) as in (**a**–**d**), but for the composites during E2 (2002–2014) and the epochal differences between the two periods (E1 minus E2). Shaded and bold vectors represent the epochal changes (between E1 and E2) in OLR and moisture flux and are statistically significant at the 95% confidence level according to two-tailed *t*-test. Solid and dashed green contours delineate 0-value stream function at 700 hPa during E1 and E2, respectively. Letter "A" in the right panels marks the center of anticyclonic anomaly.

A closer look at the evolutions of these EASM systems reveals some differences between E1 and E2. For the earlier-onset epoch (Figure 3a–d), the suppressed convection and associated WNP subtropical high extended westward around 120° E in early June (pentads 30–33). In contrast, the WNP subtropical high was confined to the east, of 130° E, during pentads 30–31 in E2 (Figure 3e,f). It gradually strengthened and moved westward from pentad 32 to pentad 33 (Figure 3g,h). The westward extension and enhancement of the WNP subtropical high have been identified as a critical factor for Meiyu onset [3,4], due to abundant moisture being transported from the tropics toward the Yangtze River Basin by the enhanced southerly/southwesterly at the southern periphery of the WNP subtropical high. In Figure 3i–l, the enhanced WNP subtropical high in E1 was conducive to the anomalously increased moisture fluxes toward the Yangtze River Basin for Meiyu onset in early June. One may wonder whether the extension of the WNP subtropical high was also the key process accounting for the delayed onset in the mid-1960s to mid-1970s (Figure 1). We compared the evolution of large-scale circulation in 1963–1976 (not shown) and found consistent features, as seen in 2002–2014. The WNP subtropical high tended to be confined to the east of 125° E during early June of 1963–1976, which led to less moisture conveyed toward the Yangtze River Basin.

In the upper troposphere, the subtropical westerly jet and South Asian high were also enhanced and established in early June during E1 (Figure 4a–d). They showed a weaker amplitude at the same period of pentads 31–33 during E2 (Figure 4e–h). Thus, a large anomaly appeared to the south of the enhanced westerly jet (marked by "A") in pentad 30 (Figure 4i). It was strengthened and moved northwestward over the Yangtze River area in the subsequent period, from pentads 31–33, conducive to the ascending motion anomaly there (Figure 4j–l). The large-scale circulation anomalies at both lower (Figure 3) and higher (Figure 4) levels provided a favorable circulation condition [1,6,13] for Meiyu onset over the Yangtze River Basin. Note that the WNP anticyclonic anomalies shown in the differential maps between E1 and E2 (right panels in Figures 3 and 4) were characterized by a northwestward-propagating quasi-barotropic system, with centers slightly tilted northwestward with height. The spatiotemporal evolution of the anticyclonic anomalies from pentads 30–33 is very similar to the typical features of EASM-WNP intraseasonal variability [9,29].

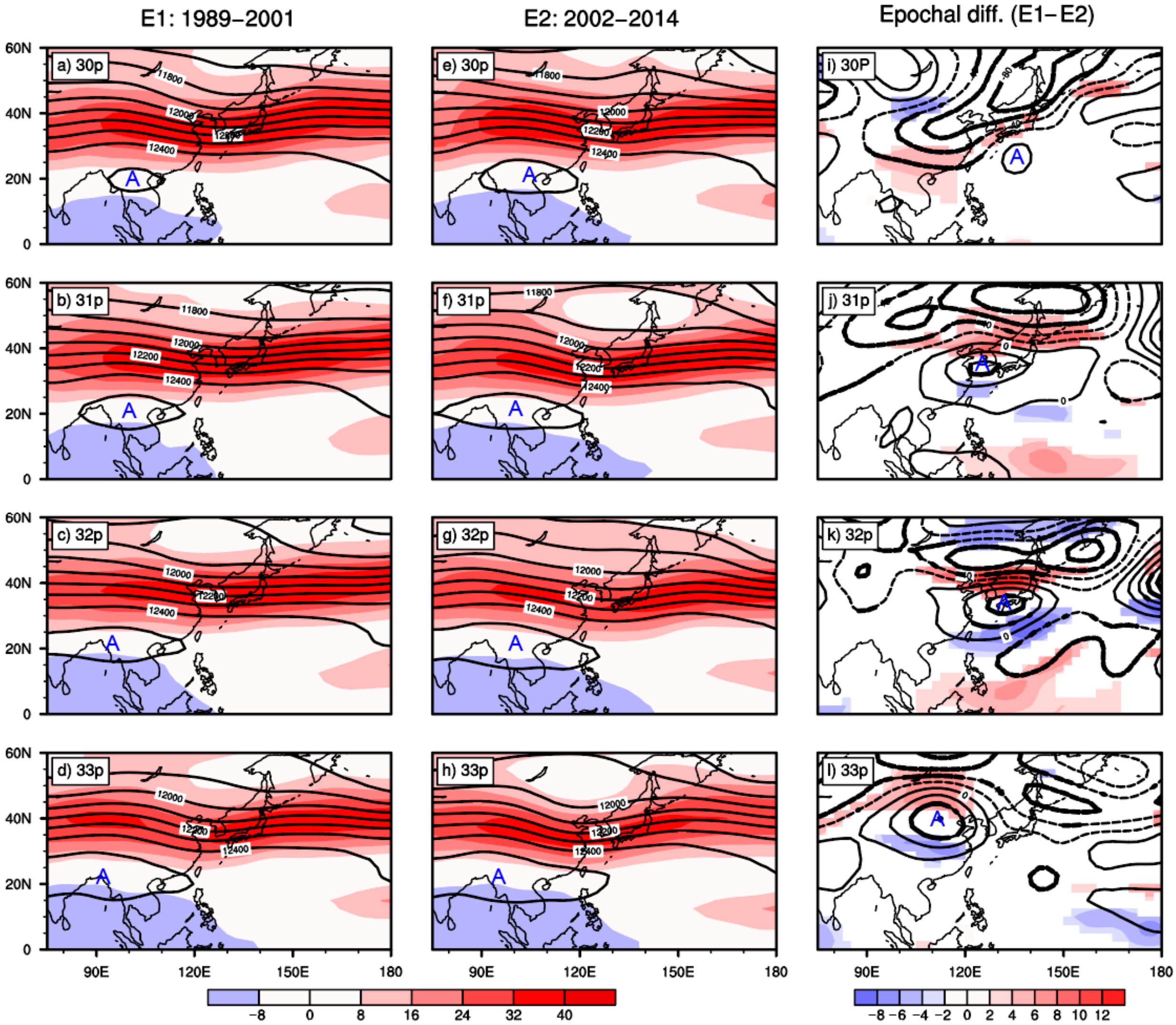

Figure 4. Composites of 200-hPa zonal wind (shading; units: m s^{-1}) and geopotential height (contour; units: m) in (**a**) pentad 30, (**b**) pentad 31, (**c**) pentad 32, and (**d**) pentad 33 during E1 (1989–2001). (**e**–**h**) and (**i**–**l**) as in (**a**–**d**), but for the composites during E2 (2002–2014) and the epochal differences between the two periods (E1 minus E2). Thick contours represent the epochal change (between E1 and E2) in 200-hPa geopotential height exceeding the 95% significance level according to two-tailed *t*-test. Letter "A" denotes the center of high pressure/anticyclonic circulation system.

To inspect whether the slowly northwestward-moving circulation anomalies that accounted for the distinct Meiyu onsets during E1 and E2 (Figures 3 and 4) are closely related to the intrinsic subseasonal components, we analyzed the CISO features in both epochs. Modulated by the annual cycle, the transient intraseasonal perturbations exhibit a phase-locking feature over the EASM region [7,9,10], as displayed in Figure 5. In both E1 and E2, the CISO-related wave trains of convection and circulation anomalies appeared over the SCS and WNP regions; they moved slowly toward East Asia from pentad 30 to pentad 33 (Figure 5a–h). The amplitude of the CISO, however, reveals a remarkable difference between E1 and E2. The CISO-associated convection and cyclonic anomalies weakened significantly in E1 compared to E2. As a result, an anticyclonic anomaly accompanied by suppressed convection is shown to move northwestward over the WNP in the difference (E1–E2) maps (Figure 5i–l).

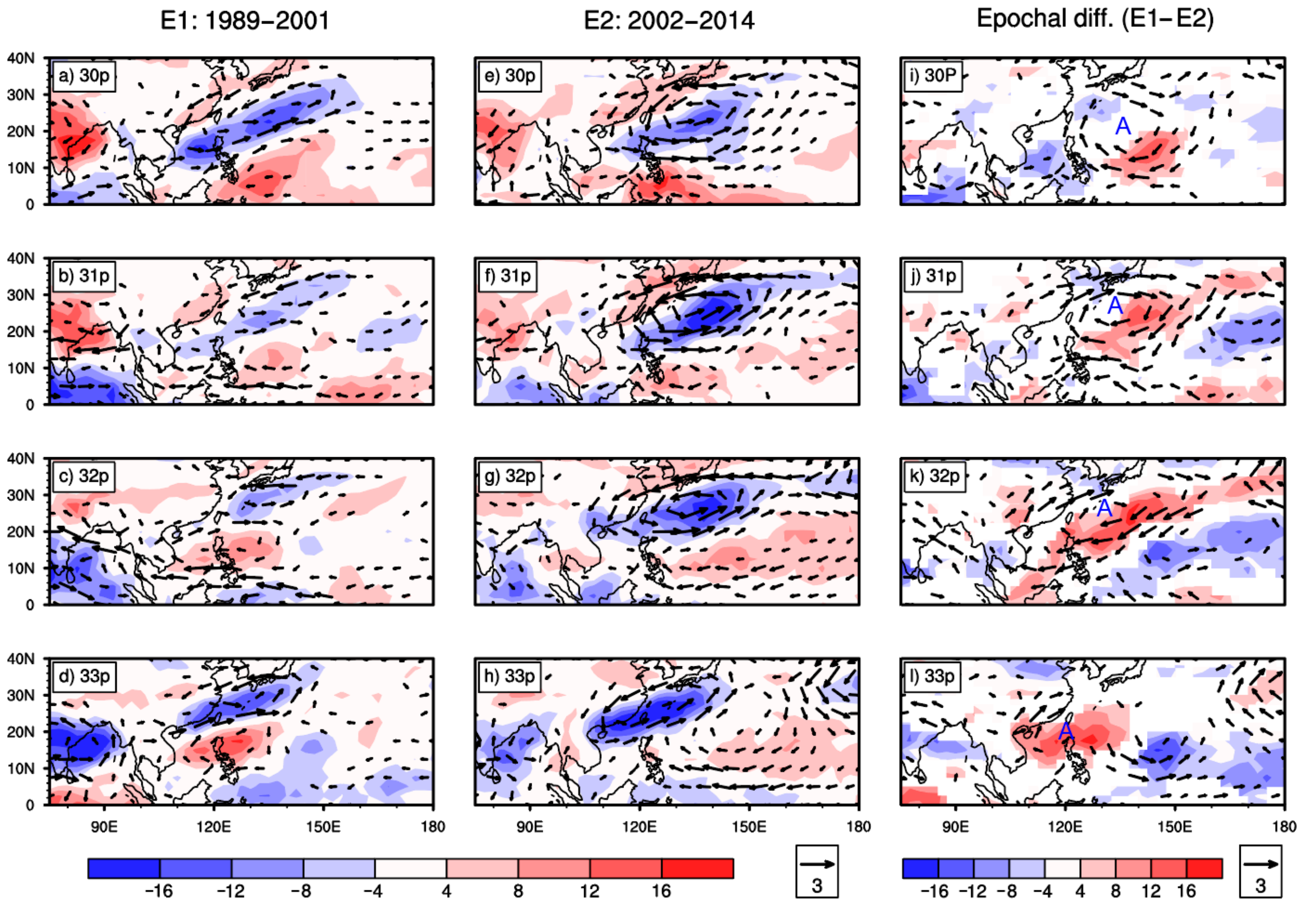

Figure 5. Composites of 20–90-day filtered OLR (shading; units: W m^{-2}) and 850-hPa wind (vector; units: m s^{-1}) in (**a**) pentad 30, (**b**) pentad 31, (**c**) pentad 32, and (**d**) pentad 33 during E1 (1989–2001). (**e**–**h**) and (**i**–**l**) as in (**a**–**d**), but for the composites during E2 (2002–2014) and the epochal differences between the two periods (E1 minus E2). Only the epochal changes (between E1 and E2) with statistical significance at the 95% confidence level, based on two-tailed *t*-test, are shown in (**i**–**l**).

Noticeably, the differential evolution of CISO-related (20–90-day) convection and circulation anomalies in early June between E1 and E2 (Figure 5i–l) is highly consistent with the epochal changes in the large-scale background conditions influencing the Meiyu onset (Figure 3i–l). The pattern correlation coefficients of convection between them (i.e., CISO in Figure 5i–l and anomalies of total OLR field in Figure 3i–l), from pentads 30–33, are 0.73, 0.72, 0.78, and 0.82, which are all statistically significant at the 95% confidence level based on two-tailed *t*-test. The results imply that the weakening of CISO convection (or suppressed convection perturbations) that propagates from the central tropical Pacific toward East Asia in early June (Figure 5i–l) contributes positively to the westward extension of the WNP subtropical high (Figure 3i–l). Along with the westward extension and enhancement of the WNP subtropical high, the low-level southerly/southwesterly anomalies that convey warm, wet air from the tropical ocean toward the Yangtze River Basin (Figures 3i–l and 5i–l) help initiate Meiyu.

Figure 6a–c show the weakening of CISO-related convection anomalies in early June of E1 compared to those in E2. The suppressed convection provided a favorable condition for the westward extension of the WNP subtropical high (Figure 6a–c). One may question if the CISO activity can explain the delayed onset in E2. To address this issue, we show the CISO patterns during pentads 34–37 (Figure 6d–f), when Meiyu initiated during E2 (Figure 1b). In mid- to late-June, the depressed CISO convection (or anticyclonic anomaly) prevailed over the subtropical WNP, with convective anomalies to its south and north sectors (Figure 6d,e). The weakened CISO intensity in E1 led to a convective/cyclonic anomaly over the WNP (Figure 6f), reducing the moisture transport from the tropics toward the Yangtze River Basin. On the contrary, the enhanced anticyclonic anomaly associated with the CISO during pentads 34–37 of E2 provided a more beneficial condition for Meiyu onset through inducing increased moisture convergence over the Yangtze River Basin (Figure 6e).

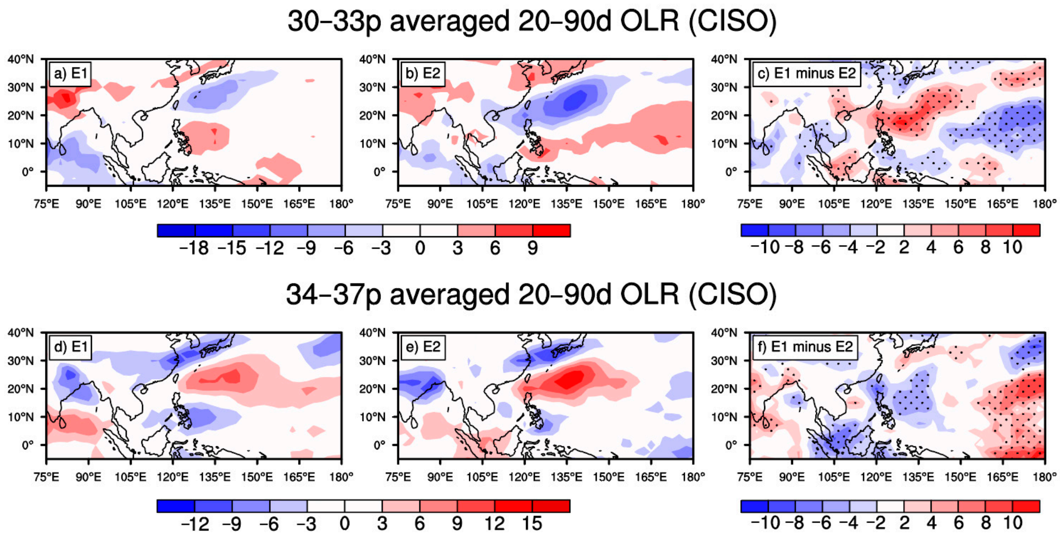

Figure 6. Amplitude of CISO-related convection (20–90-day filtered OLR; units: W m^{-2}) during pentads 30–33 of (**a**) E1, (**b**) E2 and (**c**) E1 minus E2. Stippling in (**c**) marks the region with statistically significant change at the 95% confidence level. (**d**–**f**) As in (**a**–**c**), but for the CISO during pentads 34–37.

3.2. Possible Cause of the Epochal Changes in CISO

The CISO is the climatological state of the ISO. Mechanisms responsible for the ISO variability, including background thermodynamic (such as moisture content and SST) and dynamic (i.e., vertical wind shear) conditions, are considered the factors influencing the CISO change [30]. To understand what induced the epochal differences in the WNP CISO activity, we compare the moisture content, SST and vertical wind shear during E1 and E2 (Figures 7 and 8). In early June, as the EASM starts to establish, the easterly wind shear extended from the tropical Indian Ocean to the western Pacific warm-pool region, where the low-level moisture was plentiful (Figure 7a,b). Under the vertical wind shear of the easterly, the equatorial Rossby wave tends to be enhanced, as documented in the theoretical study of Wang and Xie [30]. Thus, the tropical wind shear mainly affects the CISO at its initiation and early developing stage. The large-scale environment provided a favorable background condition for the development of the northwestward-propagating CISO over the tropical WNP [7,9,30]. Compared to E2, both the easterly wind shear and moisture were weakened in E1 (Figure 7c). This suggests that the weakened CISO activity in E1 (Figures 5 and 6) could be attributed to the less favorable environments for ISO development.

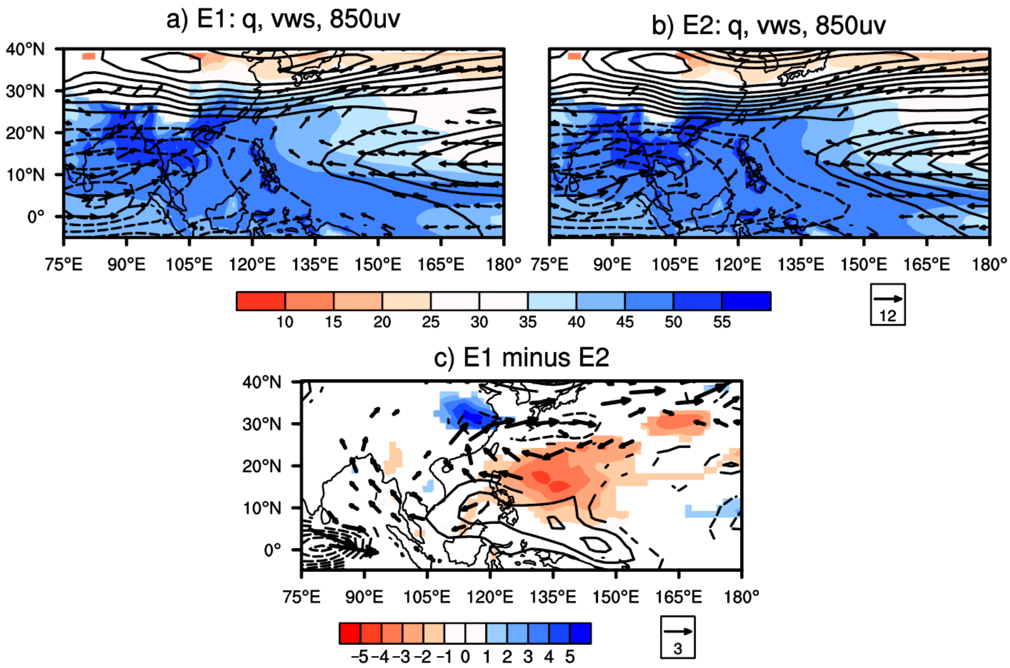

Figure 7. Similar to Figure 3, but for the composites of surface–700-hPa integrated moisture (shading; units: kg kg^{-1}), 850-hPa wind field (vector; units: m s^{-1}) and vertical wind shear (defined as 200-hPa zonal wind minus 850-hPa zonal wind; contour; units: m s^{-1}) for pentads 30–33 during (**a**) E1 and (**b**) E2, respectively, and (**c**) their differences (E1 minus E2).

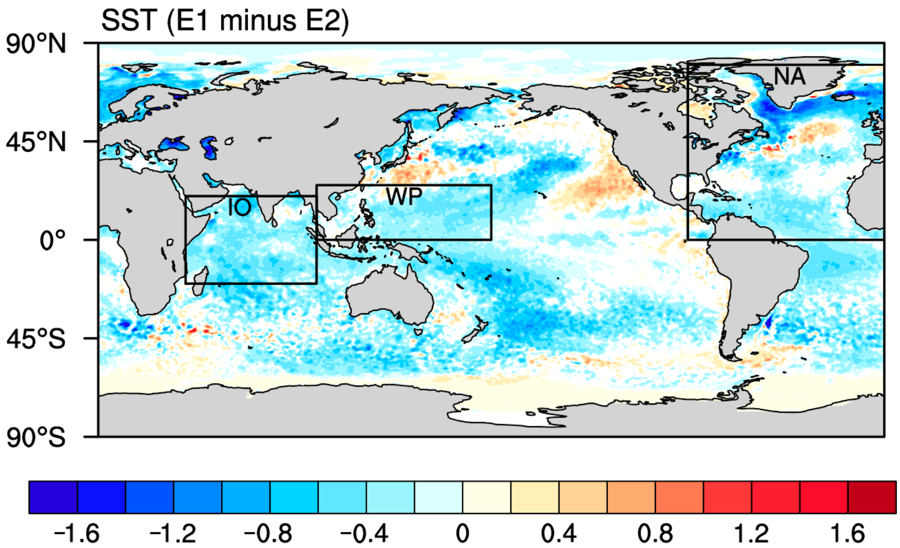

Figure 8. Epochal differences (E1 minus E2) in SST (units: K) during pentads 30–33. Only the change with statistical significance at the 95% confidence level, according to two-tailed *t*-test, is shown.

The epochal changes in these large-scale environments could be linked to the decadal SST anomalies. As expected, the reduced moisture and weakening of the easterly wind anomaly over the WNP (Figure 7c) concurred with the cold SST anomalies in early summer (Figure 8). Meanwhile, the cold SST also appeared over the Indian Ocean and most of the North Atlantic. The spring in 2002 and preceding winter were classified as neutral ENSO conditions, suggesting that the occurrence of this regime shift is not related to the ENSO.

To verify the associations of the local SST anomaly to CISO activity, we carried out AGCM experiments in which the observed SST anomalies over different basins were prescribed as boundary conditions (Table 2). A 30-year control experiment (EXP_CTRL) was conducted by prescribing the climatological monthly SST to confirm the capability of ECHAM4 AGCM in simulating the active regions of CISO variability and the background easterly wind shear over the WNP (Figure 9). Consistent with the observation (Figure 9a), the ECHAM4 simulated vigorous ISO activity over the WNP where the easterly wind share prevails (Figure 9b). Indeed, the ECHAM4 tends to overestimate the amplitude of intraseasonal variability over the warm pool region (Figure 9), as documented previously [27,31]. Numerous physical processes that regulate modeled intraseasonal variability may generate simulation biases, such as the mean state pattern, convection simulated by various cumulus parameterizing schemes, and air-sea coupling effect [32–34]. As shown in Figure 9, the enhanced intraseasonal variability concurs with increased moisture and vertical wind shear over the western tropical Pacific, suggesting the effects of mean state biases on simulated intraseasonal variability in the ECHAM4. Although the tropical intraseasonal variability is overestimated in the model, the bias would not affect the conclusions because we consider the difference in intraseasonal variability between sensitivity and control runs. The similarity between modelled and observed results suggests that the model is able to accurately portray the reality empirically.

Table 2. Boundary conditions and purposes of individual model experiments based on the ECHAM4 AGCM.

Experiment	Low Boundary Conditions	Integration Length	Purposes
EXP_CTRL	Climatological monthly SST	30 years	Assessing the simulation skill
EXP_WP	Epochal change (E1 minus E2) in SST over the western Pacific (100° E–180°, 0°–25° N) superimposed on climatological SST	20 years	Clarifying the regional SST effects on WNP background states and CISO intensity
EXP_IO	Epochal change (E1 minus E2) in SST over the Indian Ocean (40°–100° E, −20°–20° N) superimposed on climatological SST		
EXP_NA	Epochal change (E1 minus E2) in SST over the North Atlantic (90° W–0°, 0°–80° N) superimposed on climatological SST		

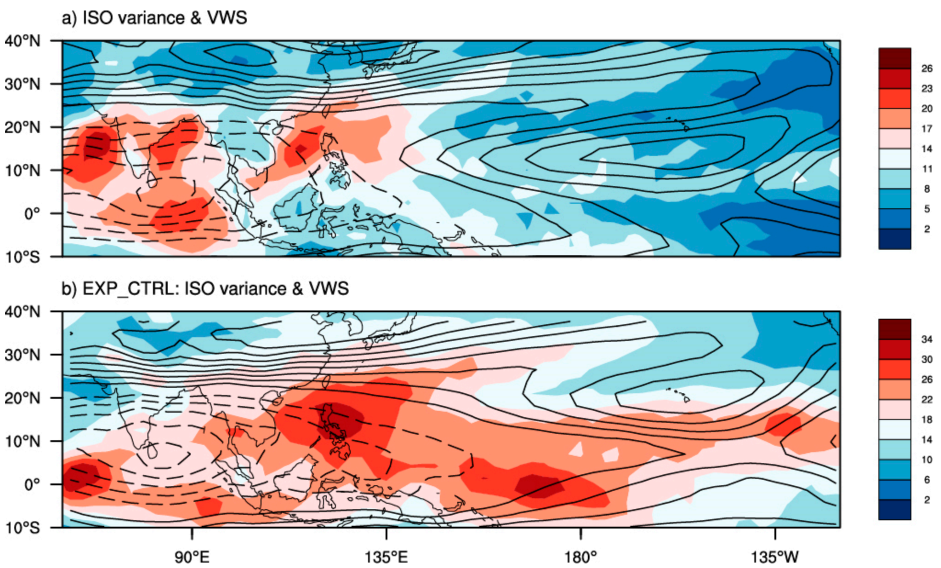

Figure 9. (**a**) Observed distributions of climatological intraseasonal (20–90-day) OLR variance (shading; units: $W^2\ m^{-4}$) and vertical wind shear (contour; units: $m\ s^{-1}$) during pentads 30–33 of 1989–2014. (**b**) Same as (**a**), but for the results derived from 30-year simulation of EXP_CTRL.

EXP_WP, EXP_IO and EXP_NA, in which regional SST anomalies over the western Pacific, Indian Ocean and North Atlantic, respectively (delineated by three boxes in Figure 8), were added to climatological monthly SST to force the model, may help elucidate the effects of decadal changes in regional SST on background conditions and associated CISO activity. The results show that in EXP_WP, the WNP CISO variability is evidently weakened (Figure 10a) under the conditions with reduced moisture and easterly wind shear (Figure 10d). However, the remote effects of Indian Ocean and North Atlantic SST anomalies on WNP CISO and background anomalies are relatively small (Figure 10b,c,e,f) compared to the local WNP SST effects. The cold SST anomalies in the two basins induce the increases in low-level moisture and easterly wind share over the WNP (Figure 10e,f), which are opposite to those observed (Figure 9a). Consequently, the ISO variability tends to be enhanced slightly (Figure 10b,c).

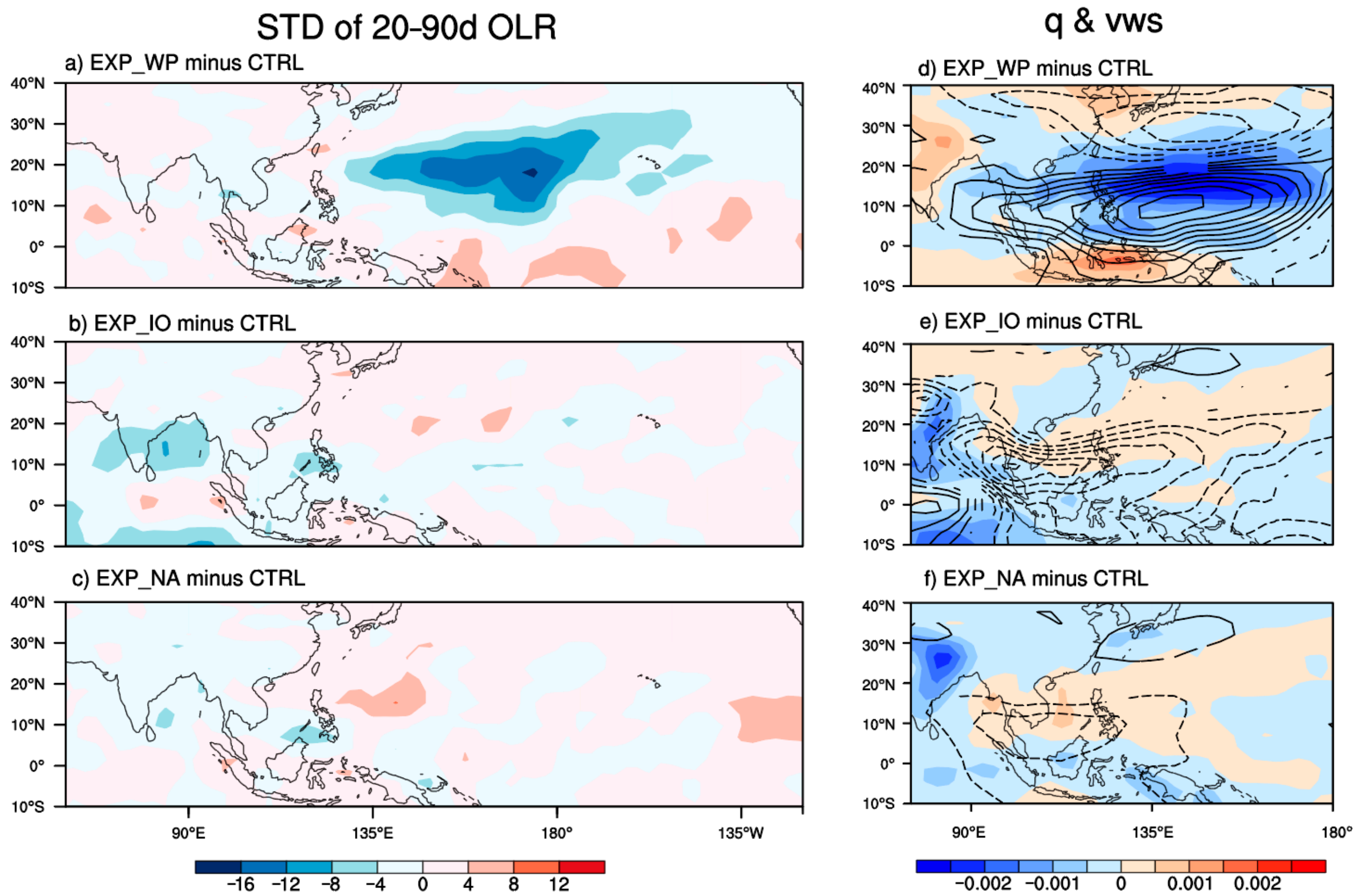

Figure 10. Effects of western Pacific, Indian Ocean, and North Atlantic SST anomalies on variability of May–June ISO convection variability and background conditions. (**a**) Difference in variability of CISO convection (i.e., standard deviation of 20–90-day OLR; units: W m^{-2}) between EXP_WP and CTRL. (**b**,**c**) Same as (**a**), but for differences in variability of CISO convection simulated by EXP_WP and EXP_NA relative to CTRL, respectively. (**d**–**f**) Same as (**a**–**c**), but for the changes in 1000–700-hPa averaged specific humidity (shading; units: kg kg^{-1}) and vertical wind shear (contour; units: m s^{-1}).

The modeling results suggest that the weakening of ISO activity in E1 is attributable to the unfavorable large-scale environment (reduced moisture content and weakened easterly wind share) accompanied by cold SST anomalies over the WNP. Due to the phase-locking nature of WNP CISO activity, the weakening of CISO convection (or a suppressed ISO anomaly/anticyclonic anomaly) appearing in early June of E1 promoted the westward enhancement of the WNP subtropical high, which favored the moisture transport and rainy season onset over the Yangtze River Basin by about two weeks earlier than that in E2 (Figures 5 and 6).

4. Discussion and Conclusions

Based on the statistical change-point analysis for Meiyu onset over the past 55 years (1960–2014), we objectively identify a regime shift around 2002. In the earlier-onset epoch (1989–2001, E1), Meiyu tended to have an earlier onset (averaged onset date on 6 June), while a delayed onset (averaged onset date on 19 June) occurred in the recent epoch (2002–2014, E2). Increased Meiyu precipitation and intensity were also identified in E1 along with the earlier onset, relative to E2, although their epochal changes are not statistically significant.

The decadal change in Meiyu onset could be attributed to the earlier (delayed) extension and enhancement of the WNP subtropical high in E1 (E2), which transported abundant moisture toward the Yangtze River Basin for the rainy season onset [1,4] in early June (mid- to late-June). The subtropical westerly jet was also enhanced, and it induced an anticyclonic anomaly to its south in early June of E1, providing an ascending motion anomaly over the Yangtze River Basin [3,6]. All these EASM-related components favor the Yangtze River Meiyu onset in early June (pentads 30–33) of E1. In contrast, the WNP subtropical high was confined to the east of 125° E in early June of E2; it showed a westward extension from mid- to late-June (pentads 34–37), consistent with the delayed onset of Meiyu in E2.

The extension and enhancement of the WNP subtropical high is closely related to the evolution and intensity of CISO activity over the WNP-EASM regions. Modulated by the annual cycle, the CISO reveals a convective (suppressed) phase fixed in early-June (mid- to late-June) over the WNP [7,9,10] while its amplitude varies at the decadal timescale. Here, we show that the CISO variability weakened remarkably in June of E1 compared to E2. As a result, the reduced (enhanced) CISO variability in E1 (E2) produced an anticyclonic anomaly in early June (mid- to late-June) over the WNP, promoting the westward extension of the WNP subtropical high and increasing moisture transport toward the Yangtze River Basin in early June (mid- to late-June). The epochal changes in CISO intensity (i.e., amplitude of intraseasonal variability) are further linked to the decadal differences in local SST and associated background conditions. The drying anomaly and reduced easterly wind shear accompanied by cold SST anomalies over the western Pacific in E1 provided an unfavorable environment for CISO development [7,30–35], which is further supported by the results of AGCM experiments in this study. The epochal changes in WNP CISO, regulated by local SST conditions at the decadal timescale, may influence the timing of Meiyu onset through modulating the timing of enhanced moisture transport toward the Yangtze River Basin by the WNP subtropical high.

The current study focused on decadal changes in Meiyu onset. How the CISO activity modulates other features of Meiyu, such as its precipitation and retreat, will be discussed in our future work. Whether the CISO serves as a potential source of Meiyu predictability at the subseasonal timescale is our ongoing work. This could advance our understanding of Meiyu predictability and help improve the skill of predicting Meiyu.

Author Contributions: Conceptualization, P.H.; software, Z.F.; formal analysis, Y.Q.; data curation, Y.L. and Q.L.; writing—original draft preparation, P.H.; writing—review and editing, P.H. and Y.Q.; visualization, Y.Q. All authors have read and agreed to the published version of the manuscript.

Funding: This research was funded by National Natural Science Foundation of China, grant number 42088101.

Institutional Review Board Statement: Not applicable.

Informed Consent Statement: Not applicable.

Data Availability Statement: The ERA-Interim data are downloadable from https://apps.ecmwf.int/datasets/data/interim-full-daily/levtype=pl/ (accessed on 18 March 2022). The SST data are downloadable from https://psl.noaa.gov/data/gridded/data.noaa.oisst.v2.highres.html (accessed on 18 March 2022). The OLR data are downloadable from https://psl.noaa.gov/data/gridded/data.interp_OLR.html (accessed on 18 March 2022).

Conflicts of Interest: The authors declare no conflict of interest.

Abbreviations

CISO	climatological intraseasonal oscillation
EASM	East Asian summer monsoon
ISO	intraseasonal oscillation
OLR	outgoing longwave radiation
SST	sea surface temperature
WNP	western North Pacific

References

1. Ding, Y.H.; Chan, J.C.L. The East Asian summer monsoon: An overview. *Meteor. Atmos. Phys.* **2005**, *89*, 117–142.
2. Gan, N. "China Has Just Contained the Coronavirus. Now It's Battling Some of the Worst Floods in Decades". Available online: https://edition.cnn.com/2020/07/14/asia/china-flood-coronavirus-intl-hnk/index.html (accessed on 14 July 2020).
3. Ding, Y.H.; Liang, P.; Liu, Y.; Zhang, Y.C. Multiscale variability of Meiyu and its prediction: A new review. *J. Geophys. Res. Atmos.* **2020**, *125*, e2019JD031496. [CrossRef]
4. Chang, C.P.; Krishnamurti, T.N. *Monsoon Meteorology*, 1st ed.; Oxford University Press: New York, NY, USA, 1987; pp. 60–92.
5. Ninomiya, K.; Shibagaki, Y. Multi-scale features of the Meiyu-Baiu front and associated precipitation systems. *J. Meteor. Soc. Jpn.* **2007**, *85*, 103–122. [CrossRef]
6. Sampe, T.; Xie, S.-P. Large-scale dynamics of the Meiyu-Baiu rainband: Environmental forcing by the westerly jet. *J. Clim.* **2010**, *23*, 113–134. [CrossRef]
7. Song, Z.H.; Zhu, C.W.; Su, J.Z.; Liu, B.Q. Coupling modes of climatological intraseasonal oscillation in the East Asian summer monsoon. *J. Clim.* **2016**, *29*, 6363–6382. [CrossRef]
8. Liu, B.Q.; Zhu, C.W. Extremely late onset of the 2018 South China Sea summer monsoon following a La Niña event: Effects of triple SST anomaly mode in the North Atlantic and a weaker Mongolian cyclone. *Geophys. Res. Lett.* **2019**, *46*, 2956–2963. [CrossRef]
9. Wang, B.; Xu, X. Northern Hemisphere summer monsoon singularities and climatological intraseasonal oscillation. *J. Clim.* **1997**, *10*, 1071–1085. [CrossRef]
10. Li, J.Y.; Liu, B.Q.; Mao, J.Y. Climatological intraseasonal oscillation in the middle–upper troposphere and its effect on the northward migration of the East Asian westerly jet and rain belt over eastern China. *Int. J. Climatol.* **2021**, *41*, 5084–5099. [CrossRef]
11. Liang, P.; Ding, Y.H. Climatology of intraseasonal oscillation of East Asia Meiyu. *Acta. Meteor. Sin.* **2012**, *3*, 418–435. (In Chinese)
12. Gu, W.; Li, C.Y.; Wang, X.; Zhou, W.; Li, W.J. Linkage between mei-yu precipitation and North Atlantic SST on the decadal timescale. *Adv. Atmos. Sci.* **2009**, *26*, 101–108. [CrossRef]
13. Zhu, J.; Huang, D.-Q.; Zhang, Y.C.; Huang, A.-N.; Kuang, X.-Y.; Huang, Y. Decadal changes of Meiyu rainfall around 1991 and its relationship with two types of ENSO. *J. Geophys. Res.* **2003**, *118*, 9766–9777. [CrossRef]
14. Sun, B.; Wang, H.J.; Zhou, B.T.; Li, H. Interdecadal variation in the synoptic features of Mei-Yu in the Yangtze River Valley Region and relationship with the Pacific decadal oscillation. *J. Clim.* **2009**, *32*, 6251–6270. [CrossRef]
15. Li, H.; He, S.P.; Fan, K.; Wang, H.J. Relationship between the onset date of the Meiyu and the South Asian anticyclone in April and the related mechanisms. *Clim. Dyn.* **2019**, *52*, 209–226. [CrossRef]
16. Yao, Y.H.; Lin, H.; Wu, Q. Linkage between interannual variation of the East Asian intraseasonal oscillation and Mei-Yu onset. *J. Clim.* **2019**, *32*, 145–160. [CrossRef]
17. Dee, D.P.; Uppala, S.M.; Simmons, A.J.; Berrisford, P.; Kobayashi, S.; Andrae, U.; Balmaseda, M.A.; Balsamo, G.; Bauer, P.; Bechtold, P.; et al. The ERA-Interim reanalysis: Configuration and performance of the data assimilation system. *Quart. J. Roy. Meteor. Soc.* **2011**, *137*, 553–597. [CrossRef]
18. Liebmann, B.; Smith, A.C. Description of a complete (interpolated) outgoing longwave radiation dataset. *Bull. Amer. Meteor. Soc.* **1996**, *77*, 1275–1277.
19. Reynolds, R.W.; Smith, T.M.; Liu, C.Y.; Chelton, D.B.; Casey, K.S.; Schlax, M.G. Daily high-resolution-blended analyses for sea surface temperature. *J. Clim.* **2007**, *20*, 5473–5496. [CrossRef]
20. Epstein, E.S. *Statistical Inference and Prediction In Climatology: A Bayesian Approach*; American Meteorological Society: Boston, MA, USA, 1985; p. 199.

21. Chu, P.-S.; Zhao, X. Bayesian change-point analysis of tropical cyclone activity: The central North Pacific case. *J. Clim.* **2004**, *17*, 4893–4901. [CrossRef]
22. Hsu, P.-C.; Chu, P.S.; Murakami, H.; Zhao, X. An abrupt decrease in the late-season typhoon activity over the western North Pacific. *J. Clim.* **2014**, *27*, 4296–4312. [CrossRef]
23. Rodionov, S.N. A sequential algorithm for testing climate regime shifts. *Geophys. Res. Lett.* **2004**, *31*, L09204. [CrossRef]
24. Duchon, C.E. Lanczos filtering in one and two Dimensions. *J. Appl. Meteor. Climatol.* **1979**, *18*, 1016–1022. [CrossRef]
25. Roeckner, E.; Arpe, K.; Bengtsson, L.; Christoph, M.; Dumenil, L.; Esch, M.; Giorgetta, M.; Schlese, U.; Schulzweida, U. *The Atmospheric General Circulation Model ECHAM-4: Model Description and Simulation of Present-day Climate*; Max-Planck Institute for Meteorology: Hamburg, Germany, 1996; p. 90.
26. Sperber, K.R.; Gualdi, S.; Legutke, S.; Gayler, V. The Madden–Julian Oscillation in ECHAM4 coupled and uncoupled general circulation models. *Climate. Dyn.* **2005**, *25*, 117–140. [CrossRef]
27. Lin, J.-L.; Kiladis, G.N.; Mapes, B.E.; Weickmann, K.M.; Sperber, K.R.; Lin, W.Y.; Wheeler, M.C.; Schubert, S.D.; Genio, A.D.; Donner, L.J. Tropical intraseasonal variability in 14 IPCC AR4 climate models. Part I: Convective signals. *J. Clim.* **2006**, *19*, 2665–2690. [CrossRef]
28. Gao, Y.X.; Hsu, P.-C.; Li, T. Effects of high-frequency activity on latent heat flux of MJO. *Clim. Dyn.* **2019**, *52*, 1471–1485. [CrossRef]
29. Tsou, C.-H.; Hsu, P.-C.; Kau, W.-S.; Hsu, H.-H. Northward and northwestward propagation of 30–60 day oscillations in the tropical and extratropical western North Pacific. *J. Meteor. Soc. Jpn.* **2005**, *83*, 711–726. [CrossRef]
30. Wang, B.; Xie, X. Low-frequency equatorial waves in vertically sheared zonal flow. Part I: Stable waves. *J. Atmos. Sci.* **1996**, *53*, 449–467. [CrossRef]
31. Fu, X.; Wang, B. Critical Roles of the Stratiform Rainfall in Sustaining the Madden–Julian Oscillation: GCM Experiments. *J. Clim.* **2009**, *22*, 3939–3959. [CrossRef]
32. Ahn, M.S.; Kim, D.; Sperber, K.R.; Kang, I.-S.; Maloney, E.; Waliser, D.; Hendon, H. MJO simulation in CMIP5 climate models: MJO skill metrics and process-oriented diagnosis. *Clim. Dyn.* **2017**, *49*, 4023–4045. [CrossRef]
33. Boyle, J.S.; Klein, S.A.; Lucas, D.D.; Ma, H.-Y.; Tannahill, J.; Xie, S. The parametric sensitivity of CAM5′s MJO. *J. Geophys. Res.* **2015**, *120*, 1424–1444. [CrossRef]
34. Kim, D.; Sperber, K.; Stern, W.; Waliser, D.; Kang, I.-S.; Maloney, E.; Wang, W.; Weickmann, K.; Benedict, J.; Khairoutdinov, M.; et al. Application of MJO simulation diagnostics to climate models. *J. Clim.* **2009**, *22*, 6413–6436. [CrossRef]
35. Hsu, P.-C.; Li, T. Role of the boundary layer moisture asymmetry in causing the eastward propagation of the Madden-Julian oscillation. *J. Clim.* **2012**, *25*, 4914–4931. [CrossRef]